High-resolution pulsed-field-ionization zero-kinetic-energy photoelectron spectroscopic study of the two lowest electronic states of the ozone cation O_3^+

S. Willitsch
Physical Chemistry, ETH Zurich, 8093 Zurich, Switzerland

F. Innocenti and J. M. Dyke
Department of Chemistry, Southampton University, Southampton SO17 1BJ, United Kingdom

F. Merkt[a)]
Physical Chemistry, ETH Zurich, 8093 Zurich, Switzerland

(Received 11 October 2004; accepted 19 October 2004; published online 23 December 2004)

The pulsed-field-ionization zero-kinetic-energy (PFI-ZEKE) photoelectron spectrum of jet-cooled O_3 has been recorded in the range 101 000–104 000 cm^{-1}. The origins of the $\tilde{X}\,^1A_1 \rightarrow \tilde{X}^+\,^2A_1$ and $\tilde{X}\,^1A_1 \rightarrow \tilde{A}^+\,^2B_2$ transitions could be determined from the rotational structure of the bands, the photoionization selection rules, the photoionization efficiency curve, and comparison with *ab initio* calculations. The first adiabatic ionization energy of O_3 was measured to be 101 020.5(5) cm^{-1} [12.524 95(6) eV] and the energy difference between the $\tilde{X}^+\,^2A_1$ (0,0,0) and $\tilde{A}^+\,^2B_2$ (0,0,0) states was determined to be $\Delta T_0 = 1089.7(4)$ cm^{-1}. Whereas the $\tilde{X} \rightarrow \tilde{X}^+$ band consists of an intense and regular progression in the bending (ν_2) mode observed up to $v_2^+ = 4$, only the origin of the $\tilde{X} \rightarrow \tilde{A}^+$ band was observed. The analysis of the rotational structure in each band led to the derivation of the r_0 structure of O_3^+ in the $\tilde{X}^+$ [$C_{2v}, r_0 = 1.25(2)$ Å, $\alpha_0 = 131.5(9)°$] and $\tilde{A}^+$[$C_{2v}, r_0 = 1.37(5)$ Å, $\alpha_0 = 111.3(38)°$] states. The appearance of the spectrum, which is regular up to 102 300 cm^{-1}, changes abruptly at $\approx$102 500 cm^{-1}, a position above which the spectral density increases markedly and the rotational structure of the bands collapses. On the basis of *ab initio* calculations, this behavior is attributed to the onset of large-amplitude motions spreading through several local minima all the way to large internuclear distances. The *ab initio* calculations are consistent with earlier results in predicting a seam of conical intersections between the $\tilde{X}^+$ and $\tilde{A}^+$ states $\approx$2600 cm^{-1} above the cationic ground state and demonstrate the existence of potential minima at large internuclear distances that are connected to the main minima of the $\tilde{X}^+$ and $\tilde{A}^+$ states through low-lying barriers. © *2005 American Institute of Physics.*
[DOI: 10.1063/1.1829974]

I. INTRODUCTION

Ozone O_3 plays a fundamental role in the physics and chemistry of the earth's atmosphere[1] and its spectroscopic properties have been studied in great detail (see, e.g., Refs. 2–4, and references cited therein). In contrast to the neutral molecule, little is known about the ozone cation O_3^+ until now. In atmospheric chemistry, the knowledge of the energy level structure of the cation is of importance for the analysis of the Rydberg spectrum of O_3 (Ref. 5) and the ion chemistry of O_3^+ (Ref. 6). Also, modeling of the role of ozone in the lower ionosphere requires direct and dissociative ionization by photons or electrons to be taken into account, and modeling of ozone in the stratosphere requires its ionization energy and electron affinity. Reliable values for the first ionization energy of O_3 and dissociation energies of O_3 and O_3^+ are central to such studies. From a spectroscopic point of view, O_3^+ is of interest as an isoelectronic species to NO_2, which has been studied intensively experimentally as well as theoretically (see, e.g., Refs. 7–9). NO_2 represents a prototypical molecular system to characterize the spectroscopic consequences of a conical intersection between two electronic states (in this case the $\tilde{X}$ and the $\tilde{A}$ state). In NO_2, the crossing point is located in the near infrared ($\approx$10 000 cm^{-1} above the ground state) and leads to extensive perturbations of the vibronic structure in the entire visible spectrum.[8]

The O_3^+ cation has been studied using conventional photoelectron spectroscopy,[10–15] photoionization mass spectrometry,[16,17] photofragment spectroscopy,[18] and electron impact ionization.[19] Already the early HeI photoelectron spectroscopic studies showed that the lowest three cationic electronic states $1\,^2A_2$, $1\,^2A_1$, and $1\,^2B_2$ are located within an energy interval of only about 1 eV (the lowest two states are almost degenerate and could not be resolved in the HeI spectra). However, the energetic ordering of these three states has not yet been unambiguously established. By an analysis of the photoelectron angular distributions, Katsumata, Shiromaru, and Kimura[14] were able to assign the highest of these

[a)]Author to whom correspondence should be addressed.

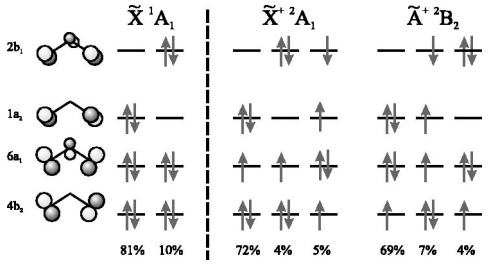

FIG. 1. Schematic molecular orbital diagram of O_3 and O_3^+ illustrating the pronounced configurational mixing of the low-lying electronic states. The percent values indicated below each configuration correspond to the results of the CASSCF calculation on O_3 (Ref. 24) and O_3^+ (see Sec. IV).

three states to the $\tilde{B}^+\,^2A_2$ state. Although the ordering of the first two states is predicted to be $\tilde{X}^+\,^2A_1$ and $\tilde{A}^+\,^2B_2$ by recent *ab initio* calculations,[20–22] this prediction remains to be confirmed by experimental measurement.

The molecular orbitals of ozone relevant for the interpretation of the photoelectron spectrum are depicted in Fig. 1. Early *ab initio* calculations of its electronic structure already showed that several configurations contribute to the electronic wave function of the ground state of O_3.[23] The leading configurations of the complete active space self-consistent field (CASSCF) wave function are[24]

$$(1a_1)^2(1b_2)^2(2a_1)^2(3a_1)^2(2b_2)^2(4a_1)^2(5a_1)^2(1b_1)^2 \times(3b_2)^2(4b_2)^2(6a_1)^2(1a_2)^2(2b_1)^0 \quad (\approx 81\%) \tag{1}$$

and

$$\cdots(4b_2)^2(6a_1)^2(1a_2)^0(2b_1)^2 \quad (\approx 10\%). \tag{2}$$

In a single-determinantal picture, the lowest three cationic electronic states $1\,^2A_2$, $1\,^2A_1$, and $1\,^2B_2$ arise from the ionization out of the $1a_2$, $6a_1$, and $4b_2$ molecular orbitals, respectively. As in the ground state of the neutral molecule, several configurations significantly contribute to the electronic wave functions of these cationic states. The CASSCF wave function of the $\tilde{X}^+\,^2A_1$ state consists of the dominant configurations (see Sec. IV)

$$\begin{aligned} &\cdots(4b_2)^2(6a_1)^1(1a_2)^2(2b_1)^0 \quad (\approx 72\%),\\ &\cdots(4b_2)^2(6a_1)^1(1a_2)^0(2b_1)^2 \quad (\approx 4\%),\\ &\cdots(4b_2)^1(6a_1)^2(1a_2)^1(2b_1)^1 \quad (\approx 5\%), \end{aligned} \tag{3}$$

and the most important configurations of the $\tilde{A}^+\,^2B_2$ state wave function are

$$\begin{aligned} &\cdots(4b_2)^1(6a_1)^2(1a_2)^2(2b_1)^0 \quad (\approx 69\%),\\ &\cdots(4b_2)^2(6a_1)^1(1a_2)^1(2b_1)^1 \quad (\approx 7\%),\\ &\cdots(4b_2)^1(6a_1)^2(1a_2)^0(2b_1)^2 \quad (\approx 4\%). \end{aligned} \tag{4}$$

Because of configuration interaction in the neutral and ionic states, and electron reorganization on ionization, the ordering of the $\tilde{X}^+\,^2A_1$, $\tilde{A}^+\,^2B_2$, and $\tilde{B}^+\,^2A_2$ states predicted theoretically does not correspond to the energetic ordering of the $4b_2$, $6a_1$, and $1a_2$ molecular orbitals of the neutral molecule.

The previous HeI photoelectron spectroscopic studies did not allow a detailed characterization of the vibronic structure of the $\tilde{X}^+$ and $\tilde{A}^+$ states. At the resolution of about $200\ \mathrm{cm}^{-1}$ achieved in these studies, the first photoelectron band consists of partially resolved features which were assigned to progressions in the bending modes of both states. The irregular spacings between the bands were either explained by Renner-Teller coupling[12] or by the large-amplitude motion in a double minimum potential.[14] The vibronic structure observed in these spectra was analyzed by Köppel, Cederbaum, and co-workers using a vibronic coupling model and analytical potentials for the $\tilde{X}^+$ and $\tilde{A}^+$ states derived from *ab initio* calculations.[20,25–27] In these studies, the irregular structure of the first photoelectron band was attributed to nonadiabatic effects in the vicinity of a conical intersection between the $\tilde{X}^+$ and $\tilde{A}^+$ states which was calculated to lie $\approx 2500\ \mathrm{cm}^{-1}$ above the minimum of the $\tilde{X}^+$ state potential.

The adiabatic ionization energy of O_3 has also not been unambiguously determined up to now. In their HeI photoelectron spectra, Dyke *et al.*[12] and Katsumata, Shiromaru, and Kimura[14] observed a weak band at 12.44 eV which was assigned to the transition to the vibronic ground state of the cation. This weak band was not observed in other studies[11,13] in which a value of 12.52 eV was reported in agreement with the result of 12.519 ± 0.004 eV obtained by photoionization mass spectrometry.[16] A value near 12.52 eV has also been suggested on the basis of an analysis of the relevant thermochemical cycles.[18,19] The simulation of the intensity distribution of the first photoelectron band led Müller, Köppel, and Cederbaum to propose that the spectral feature near 12.44 eV actually corresponds to a hot band.[27]

In the present study, the pulsed-field-ionization zero-kinetic-energy (PFI-ZEKE) photoelectron spectrum of O_3 was recorded with a resolution two to three orders of magnitude higher than in previous investigations. The high resolution enabled the observation of the rotational structure of many bands. The analysis of this structure turned out to be the key to the assignment of the vibronic symmetries of the cationic states using photoionization selection rules and allowed the unambiguous determination of the energetic ordering of the $^2A_1$ and $^2B_2$ states, of their corresponding adiabatic ionization energies, and of the lowest dissociation energy of the cation. The potential energy surface of the lowest state was explored by theoretical methods to gain insight into the mechanisms that are responsible for the complex and dense vibronic structure that is observed at excitation energies $>1500\ \mathrm{cm}^{-1}$.

II. EXPERIMENT

A detailed description of the extreme-ultraviolet (XUV) PFI-ZEKE photoelectron spectrometer has been given previously[28] and only aspects relevant to the present study are discussed here. Tunable XUV radiation in the range $101\,000$–$104\,000\ \mathrm{cm}^{-1}$ was generated by resonance-enhanced sum-frequency mixing in a xenon gas beam using the $(5p)^5(^2P_{3/2})6p[1/2](J=0) \leftarrow (5p)^6\,^1S_0$ two-photon resonance at $2\tilde{\nu}_1 = 80\,118.974\ \mathrm{cm}^{-1}$.

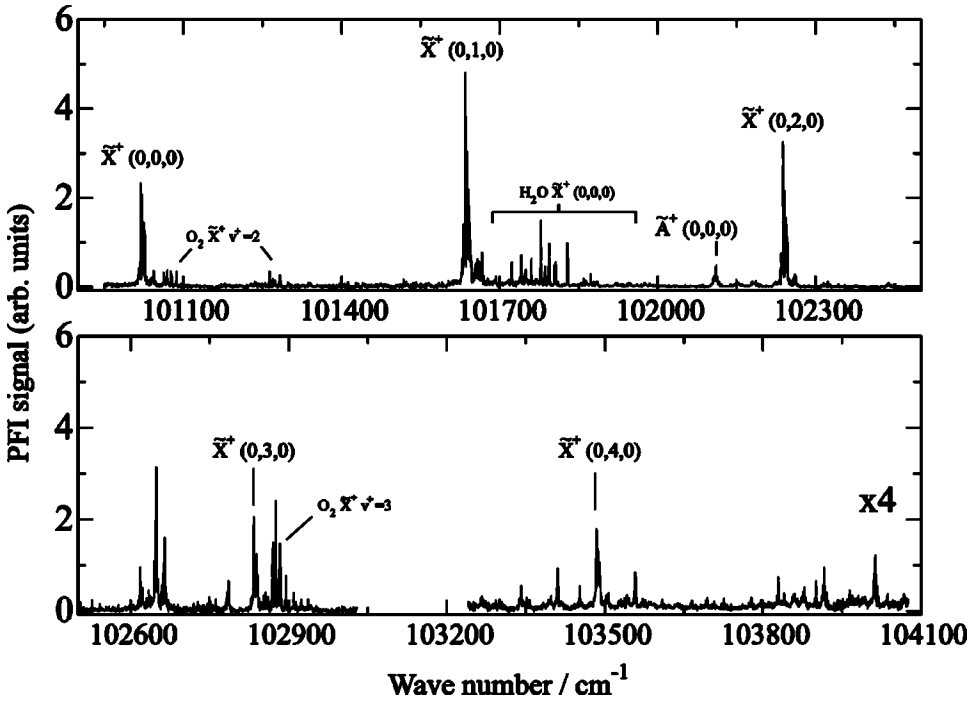

FIG. 2. Survey of the PFI-ZEKE photoelectron spectrum of jet-cooled O_3 between 101 000 and 104 000 cm^{-1}, covering the region from the first adiabatic ionization threshold to slightly beyond the predicted position of the conical intersection between the $\tilde{X}^{+\,2}A_1$ and $\tilde{A}^{+\,2}B_2$ potential energy surfaces. All observed spectral features except those explicitly assigned to O_2 and H_2O represent photoelectron bands of O_3.

Ozone was generated by a discharge of oxygen (purity 99.999%, Pangas) in a homemade ozonizer (Southampton) and stored on nonindicating silica gel in a U-tube at $-79\,^{\circ}C$. To transfer the substance into the measurement chamber, the U-tube was attached to the gas inlet of the spectrometer using glass and teflon-coated stainless steel tubing. The ozone was desorbed from the silica gel at $-15\,^{\circ}C$, seeded into a stream of helium at a pressure of 1.3 bar, and introduced into the photoionization region by means of a skimmed pulsed supersonic expansion. The rotational temperature of O_3 was determined to be $T_{rot}=6$ K from the rotational structure of the photoelectron spectra. A partial decomposition of ozone could not be avoided leading to a small amount of oxygen in the gas sample. The gas mixture was renewed before each scan.

PFI-ZEKE photoelectron spectra were recorded following single-photon XUV excitation from rotational levels of its vibronic ground state to very high Rydberg states located below the successive ionization thresholds by monitoring the wave number dependent electron signal produced by pulsed-field ionization[29] using a two-pulse electric field sequence. The first pulse with an amplitude of $+100$ mV/cm and a duration of 500 ns was triggered 500 ns after the XUV laser pulse and served the purposes of removing spurious free electrons from the photoionization region and of narrowing down the range of Rydberg states which are field ionized by the subsequent pulse.[30] The second field pulse with an amplitude of -200 mV/cm was applied immediately after the first and the electrons released by this pulse were monitored by setting a suitable detection gate in the electron time-of-flight spectrum. This pulse sequence enabled a resolution of $\Gamma_{FWHM}=0.6\ cm^{-1}$ in the PFI-ZEKE photoelectron spectra. Selected bands were recorded at a higher resolution of $\Gamma_{FWHM}=0.4\ cm^{-1}$ by decreasing the amplitude of the second pulse to -120 mV/cm.

Apart from the spectral features of ozone, the PFI-ZEKE photoelectron spectrum also contains bands of water and oxygen which appear as impurities in the gas sample. O_2 stems from the decomposition of ozone in the gas system and H_2O from moisture trapped on the silica gel. Baking the U-tube at $140\,^{\circ}C$ before each loading with ozone did not eliminate the contamination with H_2O. To distinguish the bands of ozone from those of these impurities, mass-analyzed threshold-ionization (MATI) spectra of selected bands were recorded by monitoring the wave number dependent O_3^+ ion signal generated by pulsed-field ionization of high Rydberg states[31] with a two-pulse electric field sequence. The first pulse with an amplitude of -780 mV/cm and a duration of 3.0 μs was triggered 100 ns after the vacuum ultraviolet excitation and served the purpose of separating prompt O_3^+ ions from the Rydberg molecules. The second pulse with an amplitude of $+43.1$ V/cm was used to ionize the Rydberg species and extract the ions. The MATI spectra were not as highly resolved as the PFI-ZEKE photoelectron spectra and primarily served the purpose of identifying the bands of ozone.

The absolute wave number calibration was achieved by the simultaneous recording of optogalvanic spectra of neon and making reference to the line positions tabulated in Ref. 32.

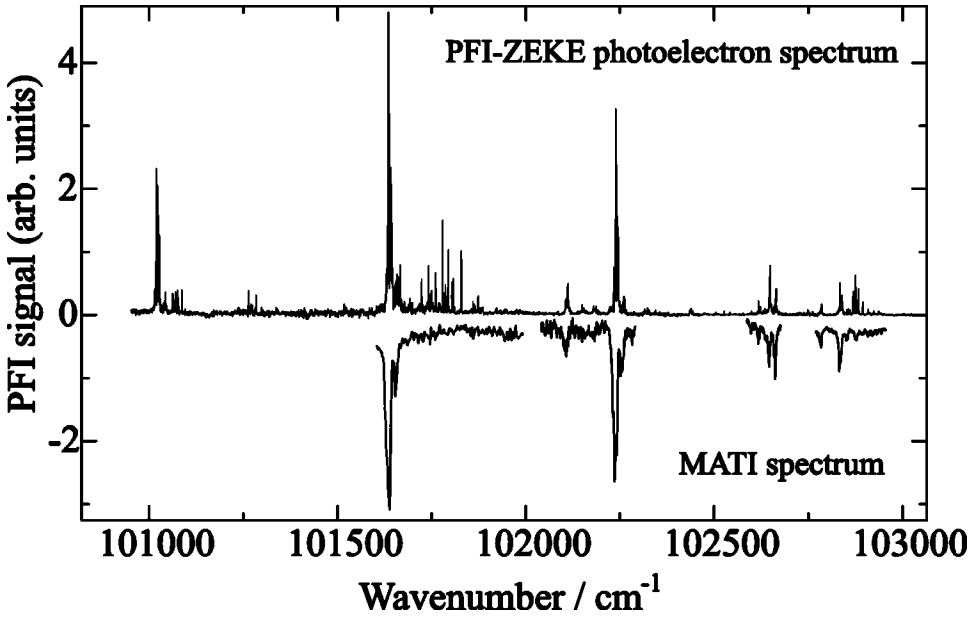

FIG. 3. Comparison of the PFI-ZEKE photoelectron and MATI spectra of O_3 demonstrating how the bands of O_3 were distinguished from impurity bands.

III. PFI-ZEKE PHOTOELECTRON SPECTRA AND THEIR INTERPRETATION

A. Vibronic structure

A survey PFI-ZEKE photoelectron spectrum of the lowest two electronic states of the ozone cation is shown in Fig. 2. The spectrum also contains bands of the impurities O_2 and H_2O, which could easily be identified by comparison with their known spectra.[33,34] These bands were not present in the MATI spectrum which is compared with the PFI-ZEKE photoelectron spectrum in Fig. 3. All other spectral structures of the PFI-ZEKE photoelectron spectrum could be attributed to ozone on the basis of the MATI spectrum and of the analysis of the rotational structures of the bands. The intensity of the XUV radiation was too low for spectra of sufficient quality to be recorded in the region from 103 000 to 103 250 cm^{-1}.[35] The intensity scale of the spectrum beyond 103 250 cm^{-1} could only be approximately matched to that of the region below 103 000 cm^{-1}.

Because of the uncertainty in the literature concerning the precise value of the first adiabatic ionization energy of O_3, special care was taken in the identification of the origin band of the PFI-ZEKE photoelectron spectrum. In Fig. 4, a detailed view of the region of the lowest band observed in the PFI-ZEKE photoelectron spectrum of Fig. 2 is compared on a larger scale with the photoionization (PI) spectrum recorded by monitoring the O_3^+ photoion signal as a function of the XUV wave number. The PI spectrum shows a clear step rising from a signal level of zero over the first PFI-ZEKE photoelectron band which indicates that this band corresponds to the first adiabatic component. The signal-to-noise ratio of our PI measurement would have been sufficiently high to observe a step in the PI spectrum corresponding to the first weak band observed at 12.44 eV by Dyke *et al.*[12] and Katsumata, Shiromaru, and Kimura.[14] We attribute this apparent contradiction to the different temperatures of the O_3 sample and conclude that the first band observed in the HeI photoelectron spectra of room temperature O_3 represents a hot band, as already suggested by Müller, Köppel, and Cederbaum.[27]

Three types of bands are observed in the PFI-ZEKE photoelectron spectrum.

First, in the low wave number region of the spectrum (see upper panel of Fig. 2), a regular progression of intense bands is observed which exhibit almost identical rotational structures and thus correspond to cationic states of the same vibronic symmetry. The average spacing of about 620 cm^{-1} between the bands is similar to the fundamental bending wave number $\tilde{\nu}_2 = 700.931\ cm^{-1}$ of neutral O_3 (Ref. 3) and corresponds well to the harmonic bending wave number of 634 cm^{-1} predicted in CASSCF(17,12)/aug-cc-pVTZ *ab initio* calculations (see Sec. IV). Hence, these bands can be confidently assigned to a progression in the bending mode $(0,v_2^+,0)$ of the $\tilde{X}^+$ state of the cation. The progression is observed up to the (0,4,0) band at 103 484 cm^{-1}.

Second, a weaker feature at 102 110 cm^{-1} is observed which possesses a different rotational structure and hence

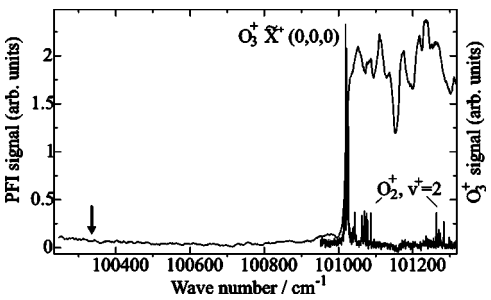

FIG. 4. Comparison of the PFI-ZEKE photoelectron spectrum (lower trace) and the photoionization spectrum (upper trace) of jet-cooled ozone showing the adiabatic onset of the $\tilde{X}\ ^1A_1 \rightarrow \tilde{X}^+\ ^2A_1$ photoelectron transition. The arrow indicates the position of the onset of the HeI photoelectron spectrum of room-temperature O_3.

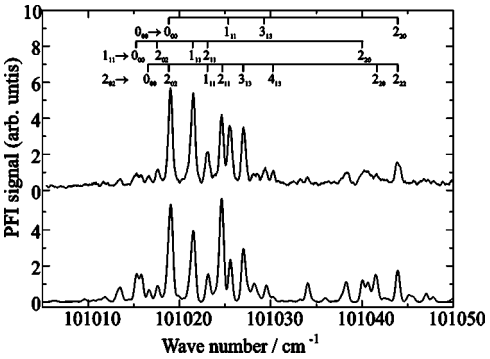

FIG. 5. High-resolution PFI-ZEKE photoelectron spectrum of the $\tilde{X}\,^1A_1\ (0,0,0) \rightarrow \tilde{X}^+\,^2A_1\ (0,0,0)$ band of O_3 showing the almost completely resolved rotational structure (top trace). The transitions are labeled using the notation $N''_{K''_aK''_c} \rightarrow N^+_{K^+_aK^+_c}$. The lower trace represents a simulation of the spectrum based on a quantitative model for the rotational line intensities in the photoelectron spectra of asymmetric top molecules.

must be attributed to a cationic state of a different vibronic symmetry than the bands of the bending progression in the $\tilde{X}^+$ state. This band was assigned to the origin band of the $\tilde{A}^+$ state $[\tilde{A}^+\ (0,0,0)]$ on the basis of an analysis of the rotational structure as will be discussed in detail in Sec. III B 2. No other band showing a similar rotational structure could be identified in the entire spectrum.

Third, the spectrum in the region $>102\,600\ \mathrm{cm}^{-1}$ is dominated by a multitude of narrow features. Their rotational structures are all similar but are very different from those of the $\tilde{X}^+\ (0,v_2^+,0)$ and $\tilde{A}^+\ (0,0,0)$ bands. As will be discussed in Sec. IV, the vibronic structure in this region of the spectrum is likely to be strongly influenced by the nonadiabatic coupling between the $\tilde{X}^+$ and $\tilde{A}^+$ states and by large-amplitude motions. Because of the high density of vibronic states and the very irregular appearance of the spectrum, no conclusive assignment of these bands could yet be reached.

B. Rotational structure

1. The $\tilde{X}^+\,^2A_1\ (0,v_2^+,0)$ bands

A detailed view of the first band in the PFI-ZEKE photoelectron spectrum is shown in Fig. 5. The well-resolved rotational structure has been assigned on the basis of an analysis of lower state combination differences and of simulations of the rotational structure after successive refinements of the ionic rotational constants.

In Table I, the rotational selection rules for photoionizing transitions from the vibronic ground state of neutral O_3 to vibronic states of the cation with symmetry Γ^+_{ve} are given in terms of the changes of the asymmetric top quantum numbers $\Delta K_a = K_a^+ - K_a''$ and $\Delta K_c = K_c^+ - K_c''$. The selection rules have been derived from the general rovibronic photoionization selection rules[36] in the molecular symmetry (MS) groups $C_{2v}(M)$ and $C_s(M)$. The linear configuration [with its corresponding symmetry group $D_{\infty h}(M)$] is not accessible in the cation at the excitation energies of less than 4000 cm^{-1} investigated in the present study[20] and is hence not considered further. Because the electronic symmetries Γ_e^+ of the first two cationic states are A_1 and B_2 in $C_{2v}(M)$ and the symmetries of the normal modes are also either a_1 (symmetric stretch ν_1 and bend ν_2) or b_2 (asymmetric stretch ν_3), only vibronic states with symmetries $\Gamma^+_{ve} = A_1$ and B_2 need to be considered. Both of these irreducible representations correlate with A' in $C_s(M)$. From Table I, it can be seen that the rotational photoionization selection rules vary according to the vibronic symmetry of the cationic state and the MS group in which they are derived. Thus, by an analysis of the rotational structure it is possible to determine the vibronic symmetry of the cationic state and the relevant MS group.

The assignment bars in Fig. 5 denote the most intense transitions using the notation $N''_{K''_aK''_c} \rightarrow N^+_{K^+_aK^+_C}$, where N represents the quantum number of the total angular momentum without spin and $''$ and $+$ denote the neutral and ionic states, respectively. Only transitions with $\Delta K_a \Delta K_c = \mathrm{ee}$ and oo have been observed, which indicates that the vibronic symmetry of the cationic state is $\Gamma^+_{ve} = A_1$ and that the symmetry group is $C_{2v}(M)$ (see Table I). Because the symmetry of the vibrational ground state is always A_1, it is straightforward to determine the electronic symmetry of the cationic state to be A_1. Thus, the analysis of the rotational structure of the high-resolution photoelectron spectrum enabled the assignment of the symmetry of the lowest electronic state of O_3^+ based solely on experimental data.

The rotational structure was analyzed in terms of a rigid asymmetric rotor Hamiltonian for the neutral and the cationic states:

$$\mathbf{H}_{\mathrm{rot}} = A\mathbf{N}_a^2 + B\mathbf{N}_b^2 + C\mathbf{N}_c^2 . \tag{5}$$

The rotational constants A^+, B^+, and C^+ of the cationic state and the adiabatic ionization energy (corresponding to the $0_{00} \rightarrow 0_{00}$ transition) were fitted to the experimental line

TABLE I. Rotational selection rules in terms of changes of the asymmetric top quantum numbers ΔK_a and ΔK_c for photoionization transitions from the $\tilde{X}\,^1A_1\ (0,0,0)$ vibronic ground state of neutral O_3 to cationic levels with vibronic symmetries Γ^+_{ve}. The selection rules have been derived in the molecular symmetry (MS) groups $C_{2v}(M)$ and $C_s(M)$. ℓ denotes the orbital angular momentum quantum number of the photoelectron.

		ℓ even		ℓ odd		
MS group	Γ^+_{ve}	ΔK_a	ΔK_c	ΔK_a	ΔK_c	Mode
$C_{2v}(M)$	A_1	Odd	Odd	Even	Even	ν_1, ν_2
	B_2	Even	Odd	Odd	Even	ν_3
$C_s(M)$	A'	Even, Odd	Odd	Even, Odd	Even	ν_1, ν_2, ν_3

TABLE II. Adiabatic ionization energies of ozone corresponding to the formation of the $\tilde{X}^+\,^2A_1$ and $\tilde{A}^+\,^2B_2$ states of O_3^+ and rotational constants for the $\tilde{X}^+\,^2A_1$ (0,0,0) and $\tilde{A}^+\,^2B_2$ (0,0,0) states of O_3^+.

	$\tilde{X}^+\,^2A_1$	$\tilde{A}^+\,^2B_2$
IE[a]/hc (cm^{-1})	101 020.5(5)	102 110.1(6)
A^+ (cm^{-1})	5.99(10)	2.65(26)
$\frac{1}{2}(B^+ + C^+)$ (cm^{-1})	0.398(24)	0.41(10)

[a]Adiabatic ionization energy corrected for the field-induced shift of the ionization thresholds $\Delta\tilde{\nu} = -1.28(45)$ cm^{-1}.

positions at fixed values of the neutral state constants A'', B'', and C''.[2] The results of the fit are listed in Table II. The values of the fitted B^+ and C^+ constants were identical within the statistical uncertainty so that only the mean value $(B^+ + C^+)/2$ is given. The adiabatic ionization energy was determined to be IE/$hc = 101\,020.5(5)$ cm^{-1}. Assuming C_{2v} symmetry, an experimental r_0 geometry was derived from the rotational constants [bond length $r_0 = 1.250(20)$ Å, bond angle $\alpha_0 = 131.49(91)°$].

The lower trace of Fig. 5 represents a simulation of the rotational structure using the fitted rotational constants and a recently developed model for the rovibronic photoionization cross sections σ of asymmetric top molecules:[37]

$$\sigma \propto \rho'' q_v^2 \sum_{|\lambda''| \leq \ell''}^{\infty} \frac{2N^+ + 1}{2\ell'' + 1} \left[\sum_{K^+, K''} (-1)^{K^+} \times c_{K^+}^{N^+, K_a^+, K_c^+} c_{K''}^{N'', K_a'', K_c''} \begin{pmatrix} N^+ & \ell'' & N'' \\ -K^+ & \lambda'' & K'' \end{pmatrix} \right]^2 \times |C_{\ell'', \lambda''}^{(\alpha'')}|^2 [\ell'' |F_{\alpha'' \ell''}^{E, \ell''-1}|^2 + (\ell''+1)|F_{\alpha'' \ell''}^{E, \ell''+1}|^2]. \quad (6)$$

Equation (6) relies on the assumption that the photoelectron is ejected out of a definite molecular orbital $\phi_{\alpha''}$, which is expressed as a single-center expansion at the molecular center of mass with the expansion coefficients $C_{\ell'', \lambda''}^{(\alpha'')}$. ℓ'' and λ'' are the quantum numbers of the orbital angular momenta of the components of the single-center expansion and their projection on the molecular axis. q_v^2 stands for the vibrational part of the transition moment and c_K^{N, K_a, K_c} represent the expansion coefficients of the asymmetric top wave function in a symmetric top basis $|N, K\rangle$, where K denotes the quantum number of the molecule-fixed projection of **N**. ρ'' is the population of the lower state which is expressed as a product of the nuclear spin statistical weight and a Boltzmann factor. $F_{\alpha'' \ell''}^{E, \ell''\pm 1}$ represent radial transition integrals as defined in Eq. (25) of Ref. 38. Given that for the present purpose only relative rotational line intensities are of interest, the electronic factors $B_{\ell'', \lambda''}^{(\alpha'')} = |C_{\ell'', \lambda''}^{(\alpha'')}|^2 [\ell'' |F_{\alpha'' \ell''}^{E, \ell''-1}|^2 + (\ell''+1)|F_{\alpha'' \ell''}^{E, \ell''+1}|^2]$ are treated as effective parameters and are adjusted to reproduce the experimental spectrum. Angular momentum contributions of other configurations in the configuration interaction (CI) wave function are taken into account indirectly if they make a contribution to the $B_{\ell'', \lambda''}^{(\alpha'')}$ coefficients.

In the simulation of the $\tilde{X}^+$ (0,0,0) band, it was initially assumed that photoionization occurs out of the $6a_1$ molecular orbital, because the CI expansion of the electronic wave function of the cationic state is dominated by the $\cdots(4b_2)^2(6a_1)^1(1a_2)^2(2b_1)^0$ configuration (see Sec. I). The $6a_1$ orbital exhibits a strongly mixed angular momentum composition (see Fig. 1) and the single-center expansion converges slowly. The best agreement with the experimental spectrum could be achieved by taking into account a total of seven angular momentum components (ℓ'', λ''): (0,0) (with the coefficient $|B_{0,0}^{(6a_1)}| = 0.16$), (1,0) ($|B_{1,0}^{(6a_1)}| = 0.29$), (1,±1)($|B_{1,\pm 1}^{(6a_1)}| = 0.29$), (2,0)($|B_{2,0}^{(6a_1)}| = 0.29$), (2,±1) ($|B_{2,\pm 1}^{(6a_1)}| = 0.29$), (2,±2)($|B_{2,\pm 2}^{(6a_1)}| = 0.24$), and (3,±1) ($|B_{3,\pm 1}^{(6a_1)}| = 0.29$). Because of the large number of terms in the single-center expansion and the spectral congestion of the experimental spectrum, the coefficients $B_{\ell'', \lambda''}^{(\alpha'')}$ could only be determined with an accuracy of about 20%.

The good agreement between the simulated and experimental spectra confirms the predicted mixed angular momentum composition of the $6a_1$ molecular orbital and indicates that the photoelectron is ejected as a superposition of even and odd partial wave components with significant contributions up to $\ell = 4$.

The results of the analysis of the rotational structures of the bands associated with transitions to excited bending levels $(0, v_2^+, 0)$ of the $\tilde{X}^+$ state are listed in Table III. The A^+ rotational constants of the (0,3,0) and (0,4,0) bands are considerably smaller than those of the (0,0,0), (0,1,0), and (0,2,0) bands, which suggests that the rotational structures of these higher excited bending levels are probably perturbed. Moreover, the wave number difference between the (0,4,0) and (0,3,0) bands is larger than the fundamental bending wave number (see Table III). Possible causes for these perturbations are discussed in Sec. IV.

TABLE III. Rotational constants and positions relative to the ground vibronic state of the bending levels $(0, v_2^+, 0)$ of the $\tilde{X}^+\,^2A_1$ state of O_3^+.

Band	$\tilde{\nu}_0$[a] (cm^{-1})	$\Delta\tilde{\nu}_0(v_2^+, v_2^+ - 1)$[b] ($cm^{-1}$)	A^+ (cm^{-1})	$\frac{1}{2}(B^+ + C^+)$ (cm^{-1})
(0,0,0)	0	0	5.99(10)	0.398(24)
(0,1,0)	616.8(6)	616.8(6)	6.21(13)	0.40(14)
(0,2,0)	1219.9(5)	603.1(5)	5.87(13)	0.390(95)
(0,3,0)	1815.3(6)	595.4(5)	5.35(14)	0.38(11)
(0,4,0)	2465.5(6)	650.3(6)	5.43(18)	0.39(12)

[a]Wave number difference with respect to the $\tilde{X}^+\,^2A_1$ (0,0,0) band.
[b]Wave number difference $\tilde{\nu}_0(0, v_2^+, 0) - \tilde{\nu}_0(0, v_2^+ - 1, 0)$.

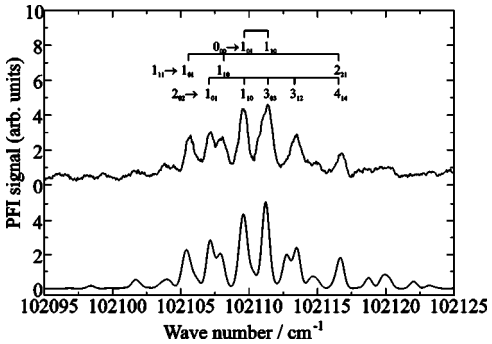

FIG. 6. High-resolution PFI-ZEKE photoelectron spectrum of the $\tilde{X}\,^1A_1\,(0,0,0)\rightarrow\tilde{A}^+\,^2B_2\,(0,0,0)$ band of O_3 showing partially resolved rotational structure (upper trace). The transitions are labeled using the notation $N''_{K''_aK''_c}\rightarrow N^+_{K^+_aK^+_c}$. The lower trace represents a simulation of the spectrum based on a quantitative model for the rotational line intensities in the photoelectron spectra of asymmetric top molecules.

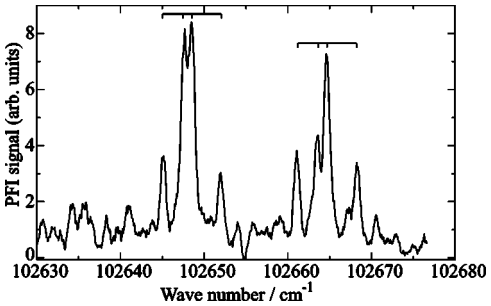

FIG. 7. High-resolution PFI-ZEKE photoelectron spectrum of O_3 in the region 102 630–102 680 cm^{-1} showing the partially resolved rotational structure typical of most bands located beyond 102 500 cm^{-1}.

2. The $\tilde{A}^+\,^2B_2$ (0,0,0) band

The PFI-ZEKE photoelectron spectrum of the $\tilde{X}\,^1A_1\,(0,0,0)\rightarrow\tilde{A}^+\,^2B_2\,(0,0,0)$ transition at 102 110 cm^{-1} is displayed in Fig. 6. The rotational structure of this band differs strongly from that of the bending progression in the $\tilde{X}^+$ state, which indicates a different vibronic symmetry of the cationic state. The assignment bars in Fig. 6 denote the most intense transitions. Only transitions with $\Delta K_a\Delta K_c$ = eo and oe are observed. Hence, it can be concluded that the symmetry group is $C_{2v}(M)$ and that the vibronic symmetry of the upper state is $\mathbf{B}_2$ (see Table I). The rotational constants and the adiabatic ionization energy were determined from a fit to the observed line positions and are listed in Table II. As for the first band, Eq. (5) was used for the neutral and cationic states. Because of the higher spectral congestion, the statistical uncertainties of the fitted parameters are larger than for the $\tilde{X}^+$ (0,0,0) band. The adiabatic ionization energy was determined to be IE/hc = 102 110.1(6) cm^{-1}. The largest rotational constant A^+ = 2.65(26) cm^{-1} is considerably smaller than for the $\tilde{X}^+$ (0,0,0) state (A^+ = 5.99(10) cm^{-1}) and the r_0 geometry derived from the rotational constants is r_0 = 1.370(52) Å and α_0 = 111.3(38)°.

The lower trace in Fig. 6 represents a simulation of the rotational structure using the fitted rotational constants and Eq. (6). It was assumed that the electron is removed from the $4b_2$ molecular orbital of the neutral molecule (the electronic wave function of the $\tilde{A}^+$ state is dominated by the $\cdots(4b_2)^1(6a_1)^2(1a_2)^2(2b_1)^0$ configuration, see Sec. I). The best agreement with the experimental spectrum could be achieved by assuming that two angular momentum components $(\ell'',\lambda'')=(1,0)$ and $(2,\pm1)$ contribute to the single-center expansion of the $4b_2$ orbital with equal weights. This implies that the photoelectron is mainly ejected as a superposition of s, d, p, and f partial waves upon ionization to the $\tilde{A}^+$ state.

From the adiabatic ionization energies, the energy difference between the $\tilde{X}^+\,^2A_1$ and $\tilde{A}^+\,^2B_2$ states can be determined to be ΔT_0 = 1089.5(4) cm^{-1}. This result is in good agreement with the theoretical value of ΔT_e = 1038 cm^{-1} (see Sec. IV).

In summary, the assignment of the band around 102 110 cm^{-1} to the origin band of the $\tilde{A}^+$ state is based on the following five observations.

(1) The vibronic symmetry of the cationic state is $\Gamma^+_{\rm ve}=B_2$.

(2) The band is the first with a rotational structure appreciably different from that of the $\tilde{X}^+$ (0,0,0) band. The $\tilde{X}^+$ (0,0,1) state also has a vibronic symmetry $\Gamma^+_{\rm ve}=B_2$; however, the theoretical harmonic wave number of $\tilde{\nu}_3$ = 838 cm^{-1} (see Sec. IV) differs too strongly from the observed wave number. Moreover, to a first approximation, the $\tilde{X}\,(0,0,0)\rightarrow\tilde{X}^+\,(0,0,1)$ band is forbidden because the vibrational overlap integral between the neutral and ionic states is zero.

(3) The observed photoionization propensity rules are compatible with photoionization out of the $4b_2$ molecular orbital of O_3.

(4) The rotational constants, and therefore the experimental r_0 geometry, agree with the results of *ab initio* calculations of the $\tilde{A}^+$ state, but differ markedly from the rotational constants and the r_e structure of the $\tilde{X}^+$ state (see Secs. III B 1 and IV).

(5) The experimental and theoretical energy difference between the $\tilde{X}^+$ and $\tilde{A}^+$ states are in good agreement (see Sec. IV).

C. Excited vibronic states beyond 102 500 cm^{-1}

The PFI-ZEKE photoelectron spectrum of two of the higher excited vibronic states is displayed in Fig. 7. The bands exhibit a distinct shape, consisting of two sharp and intense lines surrounded by two weaker satellites (see the assignment bars in Fig. 7), which is characteristic for most bands observed beyond >102 500 cm^{-1}, the only exceptions being the $\tilde{X}^+$ (0,3,0) and (0,4,0) bands at 102 834 and 103 484 cm^{-1}, respectively. The width of the partially resolved rotational structure of these bands is significantly smaller than for the $\tilde{X}^+$ $(0,v_2^+,0)$ and $\tilde{A}^+$ (0,0,0) bands, which indicates that the effective rotational constants of the upper states are considerably reduced. The strong spectral congestion prevented an unambiguous assignment and the

determination of the rotational constants A^+, B^+, and C^+ and the ionization energy IE in a fitting procedure. The rotational contour is compatible with values $A^+ < 1.0\ \mathrm{cm}^{-1}$ and $(B^+ + C^+)/2 < 0.3\ \mathrm{cm}^{-1}$. This type of band is not observed in the wave number region $< 102\,600\ \mathrm{cm}^{-1}$ suggesting that a large and abrupt change in the effective molecular geometry of the cation takes place at excitation energies of more than $1500\ \mathrm{cm}^{-1}$ with respect to the vibronic ground state. A possible explanation of this behavior will be given in Sec. IV.

D. Thermochemical implications

With the new accurate value for the first adiabatic ionization energy of O_3, a precise value of the lowest $O_3^+ \rightarrow O_2^+ + O$ dissociation threshold can be derived from a thermochemical cycle

$$D_0(O_2^+\text{-}O) = [E_{A,0K}(O_2^+, O_3) - \mathrm{IE}(O_3)]/hc = 4840 \pm 32\ \ \mathrm{cm}^{-1} (= 0.600 \pm 0.004\ \ \mathrm{eV}), \quad (7)$$

using the value of the appearance energy of O_2^+ in the photoionization of O_3^+ [$E_{A,0K}(O_2^+, O_3)/hc = 105\,860 \pm 32\ \mathrm{cm}^{-1}$ (Ref. 16)]. Alternatively, $D_0(O_2^+\text{-}O)$ can be calculated using the adiabatic ionization energy of O_2 ($\mathrm{IE}/hc = 97352.2 \pm 1.2\ \mathrm{cm}^{-1}$) (Ref. 33) and the dissociation energy of O_3 [$D_0(O_2\text{-}O) = 8566 \pm 3\ \mathrm{cm}^{-1}$]:[39]

$$D_0(O_2^+\text{-}O) = \{D_0(O_2\text{-}O) + [\mathrm{IE}(O_2) - \mathrm{IE}(O_3)]/hc\} = 4898 \pm 3\ \ \mathrm{cm}^{-1} (= 0.6073 \pm 0.0004)\ \ \mathrm{eV}. \quad (8)$$

These only slightly different results are in agreement with the previous estimate of $D_0(O_2^+\text{-}O) = 0.59$ eV given by Moseley, Ozenne, and Cosby.[18] This low value for the dissociation energy implies that O_3^+ is a very weakly bound molecule and that the ground state potential energy surface is flat and anharmonic.

IV. THEORETICAL RESULTS

A. Purpose of the *ab initio* calculations and computational methods

The purpose of the *ab initio* calculations of the potential energy surface of O_3^+ was threefold. First, they enabled a rationalization of the observed rovibronic propensity/selection rules, primarily by providing information on the molecular orbital structure of the neutral and the cation (see Secs. I and III). Second, they allowed the independent determination of the stationary points on the potential energy surfaces corresponding to the $\tilde{X}^+$ and $\tilde{A}^+$ states as well as their rotational constants and vibrational structure. This information corroborated the experimental assignments (see Sec. III B 2). Finally, the exploration of the topographic properties of the potential energy surfaces was used to establish a framework to discuss the as yet unassigned spectral features observed at excitation energies of more than $1500\ \mathrm{cm}^{-1}$ above the vibronic ground state of the cation.

The difficulties associated with accurate electronic structure calculations of neutral O_3 have been thoroughly discussed in the literature (see, e.g., Refs. 40, 41, and references cited therein). The high degree of configurational mixing in the electronic wave function necessitates a high-level treatment of static and dynamic electron correlation effects, preferably using multireference methods. The situation is analogous for the cation.[21,20] Three types of calculations have been carried out in the present investigation, which are as follows.

(1) Harmonic frequencies were calculated after geometry optimization using the complete active space self-consistent field (CASSCF) method[42,43] and the aug-cc-pVTZ basis set.[44] The active space encompassed the entire valence space [17 electrons in 12 orbitals, CASSCF(17,12)].

(2) The geometry and energy of the stationary points on the potential energy surfaces were calculated using the multireference configuration interaction method with singles and doubles excitations[45,46] (MRCI-SD) following CASSCF(17,12) calculations using the aug-cc-pVTZ basis set. In the MRCI procedure, only configuration state functions with coefficients > 0.01 were retained.

(3) Larger regions of the adiabatic potential energy surfaces of the lowest two electronic states of the cation were explored by performing single-point calculations on an equidistant grid of different nuclear configurations at the CASSCF and the multireference second-order perturbation theory (CASPT2) levels of theory.[47] The lowest two A' surfaces were calculated in C_s geometry in a state-averaged procedure with equal weights. Because these calculations also covered nuclear configurations involving large internuclear distances, a larger basis set (cc-pVQZ) was employed to reduce basis set superposition errors. To compensate for the increased computational cost, the $2s$ orbitals of the oxygen atoms were omitted from the active space in the CASPT2 calculations [CASPT2(11,9)].

All calculations were performed using the MOLPRO 2002 program package.[48]

B. Stationary points

The results for the calculations of the stationary points of the $\tilde{X}^+\,^2A_1$ and $\tilde{A}^+\,^2B_2$ states are collected in Table IV where they are compared with the present experimental results and the previous theoretical results of Schmelz *et al.*[20] Although the zero-point vibrational motion has not been accounted for in the calculations, the theoretical and experimental values for the geometries and the energy difference between the $\tilde{X}^+$ and $\tilde{A}^+$ states compare favorably, especially for the results using the MRCI method, which represents the most sophisticated method employed in the present study. As already discussed in Sec. III B 2, the good agreement between the calculated and experimental values supports the vibronic assignments of the PFI-ZEKE photoelectron spectrum, particularly with regard to the $\tilde{A}^+$ (0,0,0) band. The differences between the calculated and experimental geometries are somewhat larger for the $\tilde{A}^+$ state than for the $\tilde{X}^+$ state. We attribute this discrepancy to the pronounced anharmonicity of the potential energy surface in the vicinity of the $\tilde{A}^+$ state minimum (see Sec. IV C).

TABLE IV. Theoretical geometries, harmonic frequencies, and energy difference between the $\tilde{X}^+$ and $\tilde{A}^+$ states ΔT_e of O_3^+ calculated using different theoretical methods and the aug-cc-pVTZ basis set.

		CASSCF(17,12)	CASPT2(17,12)	MRCI[a]	Reference 20	Expt.
$\tilde{X}^+\,^2A_1$	r (Å)	1.249	1.251	1.238	1.256	1.250(20)[b]
	α (deg)	130.40	131.24	131.22	130.0	131.49(91)[b]
	$\tilde{\nu}_1$[c] (cm^{-1})	1016			1002	
	$\tilde{\nu}_2$[c] (cm^{-1})	634			592	616.8(6)[d]
	$\tilde{\nu}_3$[c] (cm^{-1})	838				
$\tilde{A}^+\,^2B_2$	r (Å)	1.291	1.297	1.283	1.290	1.370(52)[b]
	α (deg)	104.45	103.99	104.14	104.9	111.3(38)[b]
	ΔT_e (cm^{-1})	1013	976	1038		1089.7(4)[e]

[a]Only configuration state functions with coefficients >0.01 were retained in the calculation.
[b]r_0 structures.
[c]Harmonic wave number.
[d]Fundamental wave number.
[e]ΔT_0.

C. Topography of the lowest two potential surfaces

As an extension to the CASSCF calculations of the lowest two potential energy surfaces of O_3^+ performed by Schmelz *et al.*[20] in C_{2v} geometry, our calculations also covered the C_s space where the O–O bond lengths r_1 and r_2 are unequal $(r_1 \neq r_2)$.

In Fig. 8, the bending potential curves of the $\tilde{X}^+\,^2A_1$ and $\tilde{A}^+\,^2B_2$ states are shown as calculated using the CASPT2 method in C_{2v} symmetry at an O–O bond length of $r = 1.27$ Å. The minima of the potential curves were calculated at $(r,\alpha) = (1.250$ Å,$132.11°)$ and (1.288 Å, 104.05°) for the $\tilde{X}^+$ and $\tilde{A}^+$ states, respectively. Because of their different symmetries in $C_{2v}(M)$, the $\tilde{X}^+$ and $\tilde{A}^+$ states can cross and exhibit a conical intersection at $\alpha = 115.0°$ located 2600 cm^{-1} above the $\tilde{X}^+$ state minimum at a bond length of $r = 1.27$ Å. The crossing occurs at a seam along the symmetric stretching coordinate.[20] Because the $\tilde{X}^+\,^2A_1$ and $\tilde{A}^+\,^2B_2$ states correlate with the $1A'$ and $2A'$ states in C_s symmetry $(r_1 \neq r_2)$, they can interact and the crossing of the potentials is avoided as soon as the geometry deviates from the C_{2v} symmetry.

To distinguish the adiabatic from the diabatic states (which, e.g., correspond to the bending potential curves displayed in Fig. 8), the lowest two adiabatic states are labeled as $1A'$ and $2A'$. In the adiabatic picture, the potential wells corresponding to the minima of the $\tilde{X}^+$ and $\tilde{A}^+$ states are located on the lowest surface, $1A'$, and the seam of conical intersections forms a minimum energy path on the $2A'$ surface.

In Fig. 9, two-dimensional cuts through the adiabatic potential energy surface of the $1A'$ state along the r_1 and r_2 coordinates are shown for fixed values of α. These cuts have been calculated using the CASPT2 method. The potential is symmetric with respect to an interchange of r_1 and r_2. In Fig. 9(a), the bond angle was kept fixed at a value of $\alpha = 132.11°$ corresponding to the equilibrium value of the $\tilde{X}^+$ state; the minimum on the potential energy surface can be seen at $r = r_1 = r_2 = 1.240$ Å and exhibits C_{2v} symmetry. The potential energy curve along the path which corresponds to the asymmetric stretching coordinate at small displacements from the equilibrium geometry is very flat and leads, via a low-lying saddle point, to a second minimum at large internuclear distances. This path corresponds to the dissociation coordinate of the reaction $O_3^+ \rightarrow O_2^+ + O$. The minimum of the potential well corresponding to the $\tilde{X}^+$ state is only located about 1500 cm^{-1} below the saddle point which thus lies beneath the first dissociation threshold. The saddle point calculated at the MRCI/aug-cc-pVTZ level of theory is $(r_1, r_2, \alpha) = (1.354$ Å,1.198 Å,$124.282°)$ and is located

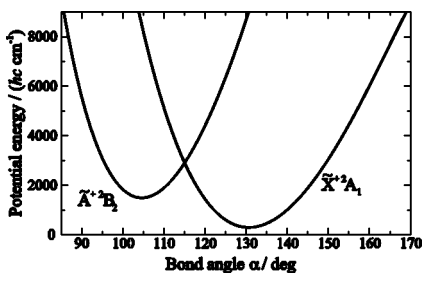

FIG. 8. Potential curves of the $\tilde{X}^+\,^2A_1$ and $\tilde{A}^+\,^2B_2$ states of O_3 along the bending coordinate. The curves were calculated for C_{2v} geometries at an O–O bond length of 1.27 Å using the CASPT2 method and the cc-pVQZ basis set.

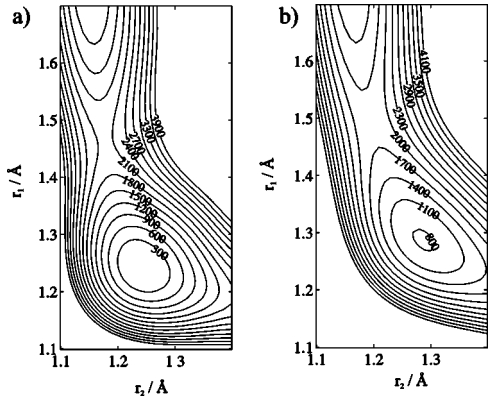

FIG. 9. Cuts through the adiabatic potential energy surface of the $1A'$ state of O_3^+ at a bond angle of (a) $\alpha = 132.11°$ and (b) $\alpha = 104.05°$ calculated at the CASPT2/cc-pVQZ level of theory. The contour values are given in cm^{-1} and are referenced to the minimum of the $\tilde{X}^+$ state.

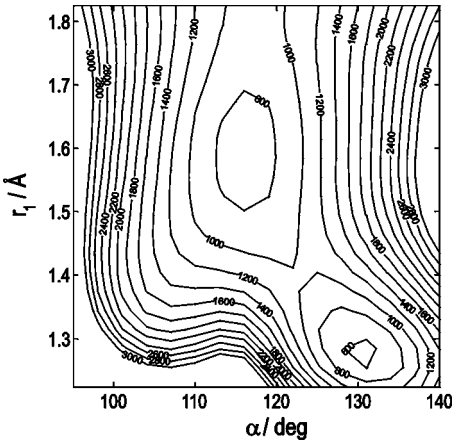

FIG. 10. Cut through the adiabatic potential energy surface of the $1A'$ state of O_3^+ at $r_2=1.20$ Å calculated at the CASSCF/aug-cc-pVTZ level of theory. The contour values are given in cm^{-1} and are referenced to the minimum of the $\tilde{X}^+$ state.

1534 cm^{-1} above the minimum of the $\tilde{X}^+$ state.

A cut at the equilibrium bond angle of the $\tilde{A}^+$ state ($\alpha=104.05°$) is shown in Fig. 9(b). The minimum of the $\tilde{A}^+$ state is located at $r=r_1=r_2=1.288$ Å and also exhibits C_{2v} symmetry. This potential well is very flat and the minimum energy path runs via a low-lying saddle point along the dissociation coordinate. The discrepancy between the experimental r_0 [1.37(5) Å, 111.3(38)°] and the calculated r_e geometries (1.283 Å, 104.14°) of this state can be attributed to the marked anharmonicity of the potential in the vicinity of the equilibrium geometry. Only one bound state could be observed experimentally in this potential well, i.e., $\tilde{A}^+$ (0,0,0).

The region around the saddle point close to the minimum of the $\tilde{X}^+$ state is displayed in Fig. 10. This cut has been calculated at the CASSCF(17,12) level of theory. The second bond length r_2 was kept fixed at $r_2=1.20$ Å and r_1 and α were varied. The potential well of the $\tilde{X}^+$ state can be discerned around $\alpha=130°$. The minimum energy path leads over the saddle point to a second minimum at large internuclear distances. The minimum corresponding to the $\tilde{A}^+$ state is not observable on this cut, but the path that leads to this minimum is discernible in the lower left corner of the figure.

The topological features of the lowest adiabatic potential energy surface provide a qualitative explanation for the sudden reduction of the rotational constants of the bands at excitation energies of more than 1500 cm^{-1} above the cationic ground state: The nuclear motion in this region is likely to spread over several wells on the potential surface and to reach into the region of large internuclear distances. We believe that this delocalization is responsible for the congested rotational structure observed in the PFI-ZEKE photoelectron spectra. First indications that the potential energy surface of the $1A'$ state is very flat were already given by Schmelz *et al.*[20] but have not been studied in detail.

In the wave number region close to the conical intersection (about 2600 cm^{-1} above the minimum of the $\tilde{X}^+$ state), nonadiabatic effects are expected to strongly influence the vibronic structure, and the nuclear motion is no longer confined to a single potential energy surface.[49,27] The high density of vibronic states observed at these excitation energies, the irregular spacings between the bands, and the apparently perturbed rotational structures of the $\tilde{X}^+$ (0,3,0) and (0,4,0) bands can thus be explained qualitatively by the complex topography of the potential energy surface and the occurrence of vibronic coupling.

The vibronic structure has already been modeled by Müller, Köppel, and Cederbaum who also considered the nonadiabatic coupling between the $\tilde{X}^+$ and $\tilde{A}^+$ states.[25–27] The calculations were performed using an analytical potential energy surface that was adjusted to the *ab initio* points calculated by Schmelz *et al.*[20] in C_{2v} geometry. A harmonic potential function was assumed along the asymmetric stretching coordinate which does not include the low-lying barriers, so that the nuclear motion was confined to relatively small displacements in r_1 and r_2. The present results show that the nuclear motion covers much larger regions of the potential energy surface already at low excitation energies and that the long-range part of the potentials must also be considered in vibronic structure calculations.

Because of the complexity of the problem, an assignment of the higher excited vibronic bands will only be possible through model calculations of the vibronic structure which take into account the nonadiabatic coupling between the $\tilde{X}^+$ and $\tilde{A}^+$ states on global potential energy surfaces. Because of the high resolution achieved in the present study, it is desirable that these surfaces be calculated with spectroscopic accuracy (a few cm^{-1}) in order to make contact with the experimental data. Such calculations have recently become possible on molecules of comparable size as has been demonstrated in the case of O_3, NO_2, H_2O and NH_3.[9,24,50,51]

V. SUMMARY AND CONCLUSIONS

The analysis of the rotationally resolved PFI-ZEKE photoelectron spectrum of O_3 has established the symmetry assignment of the lowest two electronic states of the ozone cation. The $\tilde{X}^+\,^2A_1$ and $\tilde{A}^+\,^2B_2$ states are almost degenerate with an energy difference of only $\Delta T_0=1089.7(4)$ cm^{-1}. The precise value of the adiabatic ionization energy determined here enabled the determination of a more accurate value for the lowest dissociation threshold of O_3^+ [$D_0=4898(3)$ cm^{-1}] using a thermochemical cycle. The ozone cation is thus only a very weakly bound molecule with a particularly flat and anharmonic ground state potential energy surface. The *ab initio* calculations performed in the present study show that the potential energy surfaces of the $\tilde{X}^+$ and $\tilde{A}^+$ states cross each other about 2600 cm^{-1} above the minimum of the $\tilde{X}^+$ state. In C_s symmetry, both states transform under the same irreducible representation A' and the crossing is avoided, which leads to low-lying saddle points on the adiabatic potential energy surface of the $1A'$ state. These barriers connect the potential wells of the $\tilde{X}^+$ and $\tilde{A}^+$ states with each other and with the region of large internuclear distances.

In the potential well corresponding to the $\tilde{X}^+$ state, a progression in the bending mode was observed up to $v_2^+ = 4$, whereas only one bound level was observed in the potential well corresponding to the $\tilde{A}^+$ state. The analysis of the rotational structures of the bands shows that the minima of both potential wells exhibit a C_{2v} geometry and that the rovibrational structure is regular at excitation energies up to $\approx 1200\ \mathrm{cm}^{-1}$ above the cationic ground state.

At excitation energies above $1500\ \mathrm{cm}^{-1}$, the nuclear motion starts spreading over a large region of the potential energy surface covering several minima also at large internuclear distances. The minima at large r_1 and r_2, which have been described in the present study, were not considered in earlier calculations of the vibronic structure of the $\tilde{X}^+$ and $\tilde{A}^+$ states. We believe that the dense and complex pattern of spectral features observed in this region arises from this large-amplitude motion and the nonadiabatic coupling in the vicinity of the crossing seam between the $\tilde{X}^+$ and $\tilde{A}^+$ states.

O_3^+ represents a highly interesting molecule which exhibits a very complex intramolecular dynamics already at low excitation energies: vibronic coupling between two electronic states in the vicinity of a conical intersection, large-amplitude motions covering several minima on the potential energy surface and reaching into the region of large internuclear distances, and a very low dissociation energy. The present study represents a first step toward the characterization of this complex molecular dynamics. Further theoretical studies would be desirable to aid in the understanding of the vibronic structure at higher excitation energies.

ACKNOWLEDGMENTS

The authors thank René Gunzinger for his help in the development of the apparatus, and Professor H. F. Schaefer III, Athens, and Dr. T. K. Ha, Zürich, for useful discussions concerning the *ab initio* calculations. This work was supported financially by the Swiss National Science Foundation and the ETH Zurich. J.M.D. acknowledges NERC(UK) for support.

[1] R. P. Wayne, *Chemistry of Atmospheres*, 3rd ed. (Oxford University Press, Oxford, 2000).
[2] R. Bacis, A. J. Bouvier, and J. M. Flaud, Spectrochim. Acta, Part A **54**, 17 (1998).
[3] J. M. Flaud and R. Bacis, Spectrochim. Acta, Part A **54**, 3 (1998).
[4] M.-R. De Backer-Barilly, A. Barbe, V. G. Tyuterev, and M.-T. Bourgeois, J. Mol. Spectrosc. **221**, 174 (2003).
[5] M. H. Palmer and A. D. Nelson, Mol. Phys. **100**, 3601 (2002).
[6] G. de Petris, Mass Spectrom. Rev. **22**, 251 (2003).
[7] D. K. Hsu, D. L. Monts, and R. N. Zare, *Spectral Atlas of* NO_2 *5530 to 6480 Å* (Academic, New York, 1978).
[8] B. Kirmse, A. Delon, and R. Jost, J. Chem. Phys. **108**, 6638 (1998).
[9] V. Kurkal, P. Fleurat-Lessard, and R. Schinke, J. Chem. Phys. **119**, 1489 (2003).
[10] T. N. Radwan and D. W. Turner, J. Chem. Soc. A, 85 (1966).
[11] C. R. Brundle, Chem. Phys. Lett. **26**, 25 (1974).
[12] J. M. Dyke, L. Golob, N. Jonathan, A. Morris, and M. Okuda, J. Chem. Soc., Faraday Trans. 1 **70**, 1828 (1974).
[13] D. C. Frost, S. T. Lee, and C. A. McDowell, Chem. Phys. Lett. **24**, 149 (1974).
[14] S. Katsumata, H. Shiromaru, and T. Kimura, Bull. Chem. Soc. Jpn. **57**, 1784 (1984).
[15] T. Cvitaš, L. Klasinc, and B. Kovač, Int. J. Quantum Chem. **29**, 657 (1986).
[16] M. J. Weiss, J. Berkowitz, and E. H. Appelman, J. Chem. Phys. **66**, 2049 (1977).
[17] A. Mocellin, K. Wiesner, F. Burmeister, O. Björneholm, and A. N. de Brito, J. Chem. Phys. **115**, 5041 (2001).
[18] J. T. Moseley, J.-B. Ozenne, and P. C. Cosby, J. Chem. Phys. **74**, 337 (1981).
[19] M. Probst, K. Hermansson, J. Urban *et al.*, J. Chem. Phys. **116**, 984 (2002).
[20] T. Schmelz, G. Chambaud, P. Rosmus, H. Köppel, L. Cederbaum, and H.-J. Werner, Chem. Phys. Lett. **183**, 209 (1991).
[21] N. Kosugi, H. Kuroda, and S. Iwata, Chem. Phys. **58**, 267 (1981).
[22] P. Decleva, D. De Alti, and A. Lisini, J. Chem. Phys. **89**, 367 (1988).
[23] P. J. Hay, T. H. Dunning, and W. A. Goddard, J. Chem. Phys. **62**, 3912 (1975).
[24] R. Siebert, P. Fleurat-Lessard, R. Schinke, M. Bittererová, and S. C. Farantos, J. Chem. Phys. **116**, 9749 (2002).
[25] H. Müller, H. Köppel, L. S. Cederbaum, T. Schmelz, G. Chambaud, and P. Rosmus, Chem. Phys. Lett. **197**, 599 (1992).
[26] H. Müller, H. Köppel, and L. S. Cederbaum, New J. Chem. **17**, 7 (1993).
[27] H. Müller, H. Köppel, and L. S. Cederbaum, J. Chem. Phys. **101**, 10263 (1994).
[28] F. Merkt, A. Osterwalder, R. Seiler, R. Signorell, H. Palm, H. Schmutz, and R. Gunzinger, J. Phys. B **31**, 1705 (1998).
[29] G. Reiser, W. Habenicht, K. Müller-Dethlefs, and E. W. Schlag, Chem. Phys. Lett. **152**, 119 (1988).
[30] U. Hollenstein, R. Seiler, H. Schmutz, M. Andrist, and F. Merkt, J. Chem. Phys. **115**, 5461 (2001).
[31] L. Zhu and P. M. Johnson, J. Chem. Phys. **94**, 5769 (1991).
[32] F. M. Phelps, *M.I.T. Wavelength Tables, Vol. 2, Wavelengths by Element* (MIT, Cambridge, MA, 1982).
[33] F. Merkt, R. Signorell, H. Palm, A. Osterwalder, and M. Sommavilla, Mol. Phys. **95**, 1045 (1998).
[34] Y. Song, M. Evans, C. Y. Ng, C.-W. Hsu, and G. K. Jarvis, J. Chem. Phys. **111**, 1905 (1999).
[35] R. Signorell and F. Merkt, Faraday Discuss. **115**, 205 (2000).
[36] R. Signorell and F. Merkt, Mol. Phys. **92**, 793 (1997).
[37] S. Willitsch, U. Hollenstein, and F. Merkt, J. Chem. Phys. **120**, 1761 (2004).
[38] A. D. Buckingham, B. J. Orr, and J. M. Sichel, Philos. Trans. R. Soc. London, Ser. A **268**, 147 (1970).
[39] N. Taniguchi, K. Takahashi, Y. Matsumi, S. M. Dylewski, J. D. Geiser, and P. L. Houston, J. Chem. Phys. **111**, 6350 (1999).
[40] P. Borowski, K. Andersson, P.-A. Malmqvist, and B. O. Roos, J. Chem. Phys. **97**, 5568 (1992).
[41] I. Ljubić and A. Sabljić, Chem. Phys. Lett. **385**, 214 (2004).
[42] H.-J. Werner and P. J. Knowles, J. Chem. Phys. **82**, 5053 (1985).
[43] P. J. Knowles and H.-J. Werner, Chem. Phys. Lett. **115**, 259 (1985).
[44] T. H. Dunning, J. Chem. Phys. **90**, 1007 (1989).
[45] H.-J. Werner and P. J. Knowles, J. Chem. Phys. **89**, 5803 (1988).
[46] P. J. Knowles and H.-J. Werner, Chem. Phys. Lett. **145**, 514 (1988).
[47] H.-J. Werner, Mol. Phys. **89**, 645 (1996).
[48] MOLPRO is a package of *ab initio* programs written by H.-J. Werner and P. J. Knowles, with contributions from J. Amolf, R. D. Amos, A. Berning *et al.*
[49] H. Köppel, W. Domcke, and L. S. Cederbaum, Adv. Chem. Phys. **57,** 59 (1984).
[50] H. Lin, W. Thiel, S. N. Yurchenko, M. Carvajal, and P. Jensen, J. Chem. Phys. **117**, 11265 (2002).
[51] O. L. Polyansky, A. G. Császár, S. V. Shirin, N. F. Zobov, P. Barletta, J. Tennyson, D. W. Schwenke, and P. J. Knowles, Science **299**, 539 (2003).